MWIR InAsSb $XB_n n$ detector (*bariode*) arrays operating at 150K

Philip Klipstein, Olga Klin, Steve Grossman, Noam Snapi, Inna Lukomsky, Maya Brumer, Michael Yassen, Daniel Aronov, Eyal Berkowicz, Alex Glozman, Tal Fishman, Osnat Magen, Itay Shtrichman, and Eliezer Weiss

SemiConductor Devices P.O. Box 2250, Haifa 31021, Israel

ABSTRACT

The $XB_n n$ high operating temperature (HOT) detector project at SCD is aimed at developing a HOT (~150K) mid-wave infrared (MWIR) detector array, based on InAsSb/AlSbAs barrier detector or "*bariode*" device elements. The essential principle of the $XB_n n$ *bariode* architecture is to suppress the Generation-Recombination contribution to the dark current by ensuring that the depletion region of the device is contained inside a large bandgap *n*-type barrier layer (BL) and excluded from the narrow bandgap *n*-type active layer (AL). The band profile of the $XB_n n$ device leads to effective blocking of electron transport across the BL while maintaining a free path for the holes, thus assuring a high internal quantum efficiency (QE). Our devices exhibit a very large minority carrier lifetime (~700 ns), leading to a very low dark current of $<10^{-6}$ A cm^{-2} at 150K, which is essentially diffusion limited. We compare *bariode* devices with both a *p*-type GaSb contact layer (CL) and an *n*-type InAsSb CL (termed $C_pB_n n$ and $nB_n n$, respectively). Apart from a ~0.3V shift in the operating bias, the optical and electrical properties of both architectures are virtually identical, demonstrating the generic nature of the $XB_n n$ barrier detector family. We have fabricated FPAs from $nB_n n$ *bariode* arrays bonded both to a 320×256, 30 μm pitch Read-Out Integrated Circuit (ROIC) and a 640×512, 15 μm pitch ROIC. For lattice matched FPAs the cut-off wavelength at >50% of maximum response is ~ 4.1 μm. We show an image registered at 150K with a 640×512/15 μm Pelican FPA, using f/3.2 optics. The operability at 150K is >99.5% and the measured NETD, limited only by shot and Read-Out noise, is 20 mK for a 22 ms integration time. At this f/number, the detector has a background limited performance (BLIP) up to ~165K.

Keywords: Infrared Detector, Focal Plane Array, Bariode, InAsSb, XBn, nBn, CBn, High Operating Temperature

1. INTRODUCTION

The maximum operating temperature of a solid state infrared detector is usually determined by its dark current, which increases exponentially with temperature. In standard MWIR photodiodes operating under conditions of background-limited performance (BLIP) this dark current is almost universally produced by so called Generation-Recombination (*G-R*) centres (also known as Shockley-Read-Hall traps) in the depletion region of the device. A reverse bias applied to the diode activates these *G-R* centres which provide energy levels close to the middle of the bandgap. As a result, the amount of thermal energy needed to excite an electron out of the valence band or into the conduction band is approximately halved. Electron-hole pairs are generated that are immediately removed by the electric field of the depletion region. The *G-R* current typically varies with temperature as $\sim T^s e^{-E_{GR}/k_B T}$ where E_{GR} is roughly equal to half the zero temperature semiconductor bandgap, s ~1.5 and k_B is Boltzman's constant.

In 2003, a new type of heterostructure device was proposed, termed here $CB_n n$, in which no depletion layer exists in any active narrow bandgap region[1]. "C" and "B_n" stand for contact and *n*-type barrier layers, and "*n*" for an *n*-type narrow bandgap photon absorbing layer. The contact, C, can be *p*-type ("C_p") or *n*-type ("C_n"), and can be made from either the same, or a different material, to that used for the photon absorbing layer. Devices where the same material is

used are often termed $n\mathrm{B_n}n$, when the contact is *n*-type, and $p\mathrm{B_n}n$, when the contact is *p*-type (e.g. see Ref. 2, and references therein). This family of devices, to which we have given the general name $\mathrm{XB_n}n$ (see Ref. 3), or "*n*-type *bariode*" (see Ref. 4 for an explanation and historical note), is similar in some respects to the device family proposed by White in 1983, in which two narrow gap semiconductors (not necessarily the same material) surround a *p*-type wide bandgap semiconductor, and in which a barrier only exists in the conduction band[5]. In both cases, the *n*- or *p*-type semiconductor on one side of the barrier constitutes a contact layer for biasing the device, while the *n*-type narrow bandgap semiconductor on the other side of the barrier is a photon absorbing layer whose thickness should be comparable with the absorption length of light in the device, typically several microns. The unique feature of the $\mathrm{CB_n}n$ *bariode* device in Ref. 1, is that the barrier in the $\mathrm{CB_n}n$ device contains *n*-type doping, which is tailored to ensure that the bands in the narrow bandgap photon absorbing layer are flat right up to the barrier or else contain a narrow accumulation layer immediately next to the barrier. The corresponding "*p*-type *bariode*" devices, in which all doping polarities are reversed, and in which a barrier exists only in the valence band, are termed $\mathrm{XB_p}p$, and include both $\mathrm{CB_p}p$ and $p\mathrm{B_p}p$ architectures[1]. The absence of depletion in the narrow bandgap photon absorbing layer of all *bariodes*, leads to a total suppression of the bulk *G-R* contribution to the dark current. The dark current is then limited to the diffusion contribution, which varies typically as $\sim T^s e^{-E_{\mathrm{diff}}/k_B T}$. The energy, E_{diff}, in the exponent, is close to the zero temperature semiconductor bandgap, and $s \sim 1.5$ or 3, depending on the level of doping in the active layer[6].

In conventional diodes operating in the MWIR wavelength range, the diffusion current at 77 K is typically several orders of magnitude lower than the *G-R* current, while at room temperature it is several orders greater. T_0 is defined as the "cross-over" temperature at which the diffusion and *G-R* currents are equal. Figure 1 shows a typical Arrhenius plot of the dark current in a conventional diode (solid line). The lower portion has a slope which is roughly half that of the upper portion. When multiplied by Boltzman's constant, the slopes correspond to the activation energies for *G-R* and diffusion limited behaviour respectively. The dashed line is an extension of the high temperature diffusion limited region to temperatures below T_0. It represents the behaviour of an $\mathrm{XB_n}n$ or $\mathrm{XB_p}p$ *bariode* device in which there is no *G-R* current. At temperatures below T_0, an *n*- or *p*-type *bariode* device offers two important advantages. First, it should exhibit a higher signal-to-noise ratio than a conventional diode operating at the same temperature. This is depicted by a vertical arrow in Figure 1. Second, it will operate at a higher temperature than a conventional diode with the same dark current. This is depicted by a horizontal arrow in Figure 1. *Bariode* devices also offer advantages for device fabrication. Since the barrier layer is fully depleted, it provides a natural insulator with which to isolate the pixels in a detector array. These pixels can be defined very simply by etching through the contact layer up to the barrier. It is often possible to carry out this process using a suitable selective etch. Although the process is frequently described as "passivation" free, it is necessary to apply some sort of surface chemical treatment, such as the deposition of a dielectric film, in order to avoid oxidation of the exposed barrier layer, especially if it contains aluminium (which is often the case).

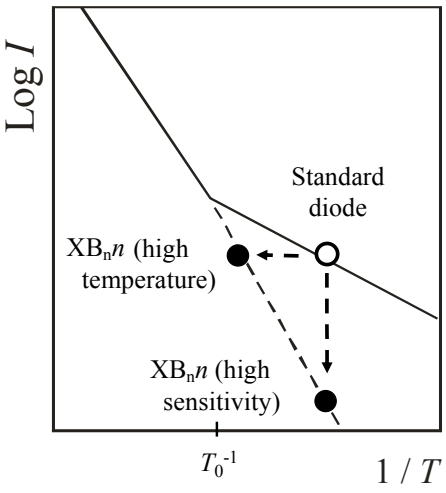

Figure 1
Schematic Arrhenius plot of the dark current in a standard diode (solid line) and in an $\mathrm{XB_n}n$ *bariode* with negligible depletion in the AL (dashed line). Open circle shows the operating point of a standard diode while solid circles show operating points for the $\mathrm{XB_n}n$ *bariode* with improved sensitivity or higher operating temperature.

In this work, we report on the electrical and optical properties of $\mathrm{C_pB_n}n$ and $n\mathrm{B_n}n$ *bariode* devices grown on a GaSb substrate, with an *n*-type Active Layer (AL) made from InAsSb, and an *n*-type Barrier Layer (BL) made from AlSbAs. In the $\mathrm{C_pB_n}n$ *bariode* the Contact Layer (CL) is *p*-type GaSb while in the $n\mathrm{B_n}n$ *bariode*, it is *n*-type InAsSb. InAsSb was chosen as the AL material, because it exhibits a high T_0 value (~180 K). As discussed in an earlier work by one of the authors[3], the value of T_0 increases with the AL bandgap, so a material such as InAsSb with a bandgap wavelength close to 4.2 μm represents a good compromise that delivers both a high operating temperature and reasonable MWIR sensitivity.

This paper is organized as follows. Some key issues in the design of *n*-type *bariode* structures are discussed in section 2, together with basic details of our wafer growth and device processing. The optical and electrical properties of single devices are discussed in section 3, followed by FPA properties in section 4. Our conclusions are summarized in section 5.

2. DESIGN, GROWTH AND PROCESSING OF DEVICE HETEROSTRUCTURES

The band profiles for C_pB_nn and nB_nn *bariode* devices under an applied bias are shown in Figure 2 (a) and (b), respectively. In Figure 2 (a), a bias lower than the optimum operating bias is shown so that a barrier for hole transport ϕ_V exists due to electron accumulation in the AL. This barrier must be surmounted in order for holes to pass into the BL. If the bias is increased, the band profile in the vicinity of the AL/BL interface will flatten until it becomes like that shown in Figure 2 (b), where ϕ_V has been reduced almost to zero. For C_pB_nn and nB_nn *bariodes* with the same BL thickness and the same AL and BL doping, it is possible to find a bias in each case where the profiles up to, but not including, the CL are identical. Thus, since this is the region of the device which determines the dark current and photo-current, we should expect very similar electro-optical performance from the two device types. Exactly such behaviour will be demonstrated in section 3. The main difference is that the operating bias (i.e. the bias that gives $\phi_V \sim 0$) in the C_pB_nn is typically a few hundred millivolts greater than for the nB_nn, due to the different valence band offsets at the CL/BL interface and the different Fermi level positions within the CL bandgap.

Bariode device heterostructures based on layers of InAsSb, AlSbAs and GaSb were designed to give band profiles similar to those shown in Figure 2. The device layers were grown on 2" *n*-type GaSb substrates in a Veeco Gen III MBE machine. After the growth of an InAsSb buffer layer, an *n*-type InAsSb AL was grown with a thickness of between 1.3 and 3 μm. The *n*-doping was in the range $1\text{-}4\times10^{15}$ cm^{-3}. Next, an *n*-type AlSbAs BL was grown with a thickness of between 0.1 and 0.3 μm. Finally, the CL (*p*-GaSb or *n*-InAsSb) was grown within a thickness in the range, 0.2-0.5 μm.

In most of the *bariodes* studied in this work the three layers (CL, BL, AL) were latticed matched with the substrate to within ~500ppm, as discussed in Refs. 6 and 7. However, in one case the AL was intentionally grown with a larger lattice mismatch in order to explore the possibility of extending the device cut-off wavelength. The results from this device are discussed in section 4.

After characterization by X-ray diffraction mapping, in order to monitor layer uniformity[6,7], the wafers were processed into square mesa structures with side dimensions of between 11 and 300 μm, or device arrays with a pitch of 15 or 30 μm. The mesas were etched to a depth slightly greater than the thickness of the CL and a common contact was

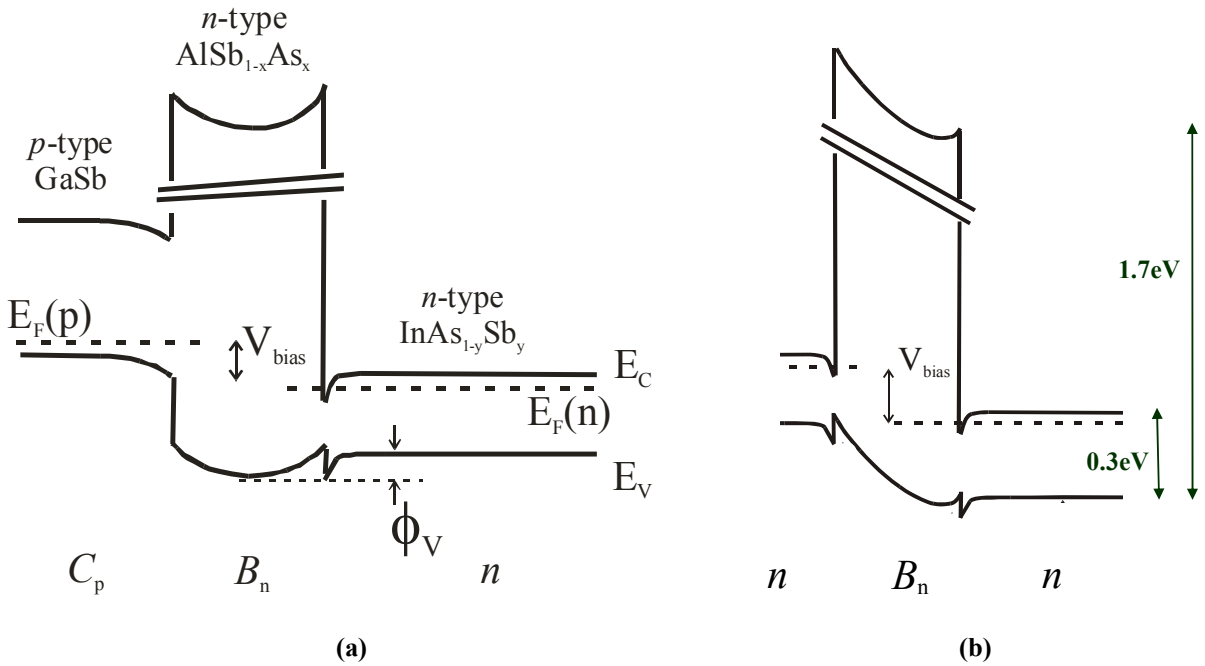

Figure 2
(a) Band profile for a C_pB_nn *bariode* made from GaSb/$AlSb_{1-x}As_x$/$InAs_{1-y}Sb_y$ when biased close to its operating voltage. The bands in the $InAs_{1-y}Sb_y$ photon absorbing layer are flat except very close to the barrier where they are accumulated. There is no depletion in this layer in contrast to the depletion that exists in both barrier and contact layers. (b) The equivalent band profile for an nB_nn *bariode* in which the *p*-GaSb contact layer has been replaced with *n*-InAsSb.

made to the back of the AL. In the case of the small test devices or the device arrays, the devices were flip chip bonded with indium bumps to a silicon Fan-Out circuit or to a silicon Read-Out Integrated Circuit (ROIC), respectively. The substrate was then polished to a thickness of a few microns and an antireflection (AR) coating was applied. The devices were characterized both electrically and optically, as described in the next two sections.

3. SINGLE DEVICE PROPERTIES

(a) Electrical properties

Large single *bariodes* were first characterized by Capacitance-Voltage measurements, in order to estimate the doping in all three of the device layers, and to confirm the BL thickness. The doping at the edge of the depletion region, whose position changes with bias, can be deduced from the derivative: $d(1/C^2)/dV$, as described in Ref. 8. This results in a doping profile plot, such as that shown in Figure 3. This Figure shows the doping profiles in the AL (reverse bias) and the CL (forward bias) for an nB_nn *bariode* with a 0.2 μm thick *n*-type BL, and a 0.2 μm thick *n*-type CL. The AL was 1.5 μm thick. The profiles for both bias directions show a rapid fall at a depth of 0.25 μm. This is close to the BL thickness of 0.2 μm. We suggest that the difference of ~0.05 μm between the measured and expected BL thickness is due to the contribution of the two accumulation layers on each side of the BL (see Figure 2(b)), where each accumulation layer behaves as an additional sheet of charge ~25-50 nm wide.

In forward bias the *C-V* profile rises rapidly at a depth of 0.4 μm, when the depletion layer meets a thin n^+ layer used to terminate the CL. This depth agrees well with the combined thickness of the BL and CL. In reverse bias, the profile shows that the doping in the AL of the device is constant and equal to ~ 4×10^{15} cm^{-3}.

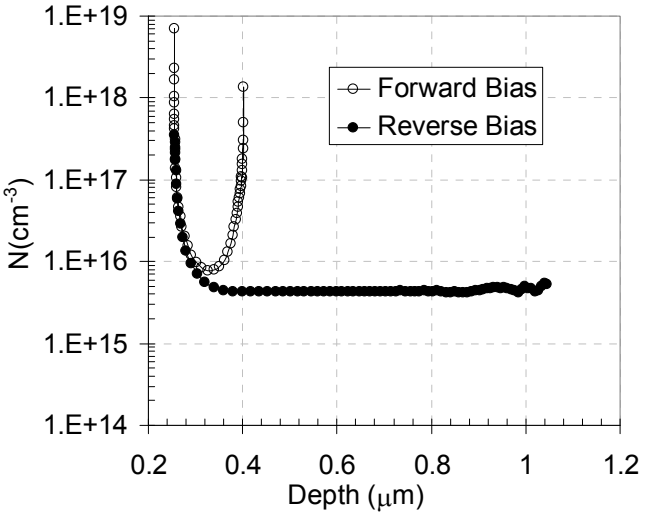

Figure 3
Doping profile, *N*, deduced from *C-V* measurements at 77K, for an nB_nn *bariode* with ~ 4×10^{15} cm^{-3} donors in the AL (Reverse Bias) and CL (Forward bias). The BL thickness was 0.20 μm. The depth scale corresponds to the position in the AL or CL measured from the far side of the BL.

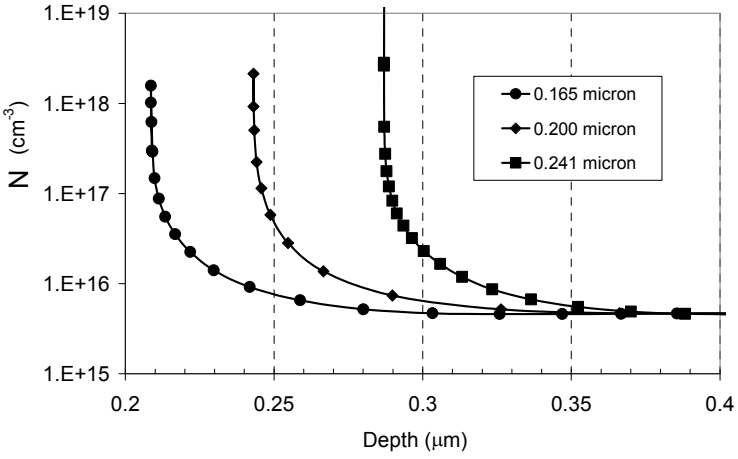

Figure 4
The left hand side of the reverse bias doping profiles for three nB_nn *bariode* devices with BL widths of 0.165, 0.20 and 0.241 μm. The AL doping in each case is the same as in Figure 3.

Figure 4 shows the beginning of three reverse bias doping profiles similar to the one shown in Figure 3, for nB_nn *bariodes* with nominal BL thicknesses of 0.165, 0.200 and 0.241μm. The shift of the left hand side of each profile corresponds well with the changes in the BL width, and confirms the accuracy of the nominal width values.

Our C_pB_nn *bariode* devices showed a very similar doping profile in reverse bias to that shown in Figure 3, with the same AL doping plateau as for the nB_nn *bariodes*. The *n*-type doping of the BL, in both the C_pB_nn and nB_nn *bariodes* has been characterized by careful modeling of the measured C-V profile near the origin, as reported previously[2].

Having characterized the doping profiles of our *bariode* devices by *C-V* measurements,

the dark current at the operating and higher bias values was measured as a function of mesa size, and temperature. At the operating bias, the bands in the AL are assumed to be close to "flat band" with ϕ_V ~0 in Figure 2. Such measurements allow us to confirm the suppression of the G-R current and to diagnose any perimeter related effects.

The straight dashed lines in the Arrhenius plots of Figure 5 show the dark current density measured at the device operating bias in (a) a C_pB_nn *bariode* with an operating bias of -0.6V and (b) an nB_nn *bariode* with an operating bias of -0.3V. The AL and BL in both devices were grown to exactly the same specifications of width and doping. These results should be compared with the solid lines in both figures, which show the device behaviour when biased to a voltage significantly higher than the operating bias. Results for both device types are shown for two mesa sizes (150 and 300 μm side dimension) and demonstrate very good uniformity.

In both types of *bariode*, the Arrhenius plots look very similar to the schematic Arrhenius plot of the dark current shown in Figure 1, with diffusion limited behaviour only at the operating bias, and a combination of G-R and diffusion limited behaviour at a somewhat higher bias. The absence of a bulk G-R current at the operating bias shows that there is very little band bending in the AL. Under these conditions, the minority holes can pass freely into the BL while at the same time there is no depletion to activate a bulk G-R current. It is shown in the next section that at the operating bias of each device, the photoresponse is saturated, confirming that all minority carriers are able to pass freely into the BL. At the high bias values, both the C_pB_nn and the nB_nn *bariodes* exhibit a strong G-R current at 150K (1000/T=6.67) because the bias is large enough to deplete part of the AL.

Figure 5 shows that at the operating bias of each device, the dark current density at 150K is 2-3×10^{-7}A/cm^{-2}, which corresponds to a dark current of just a few tenths of a pico-ampere in a pixel of a Focal Plane Array (FPA) detector with a 15 μm pitch. This should be compared with a typical photocurrent of ~12pA for an aperture of f/3 and an average Quantum Efficiency (QE) of 70% between wavelengths of 3 and 4 μm, confirming that our *bariode* detectors exhibit BLIP performance at 150K.

The low bias diffusion-related dark current curves in Figure 5, can be fitted to a dependence of the form

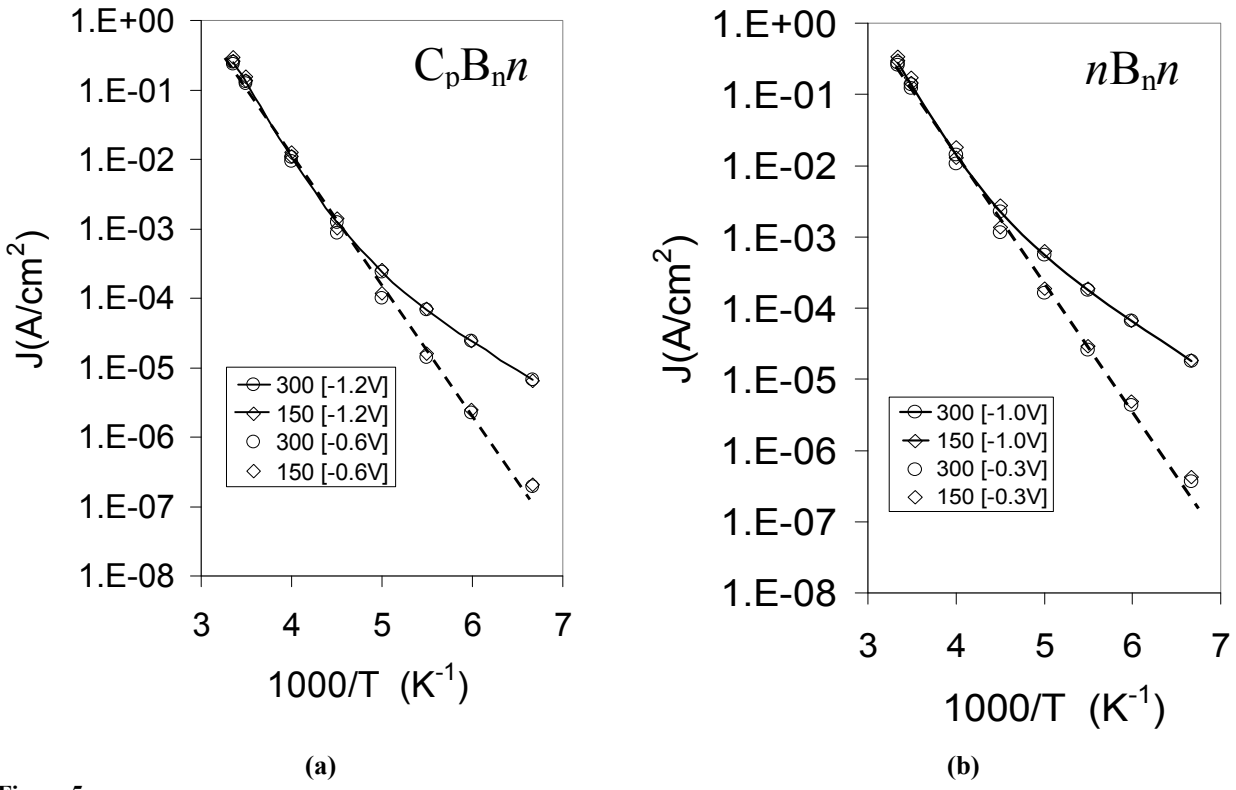

Figure 5
Arrhenius plots of the dark current density for two mesa sizes at two bias values for (a) a C_pB_nn *bariode* and (b) an nB_nn *bariode*. In each case the lower bias value corresponds to the *bariode* operating bias (at which the photoresponse saturates). The side dimensions of the different square mesa devices are shown in each legend in microns. In both cases a straight diffusion-like line (dashed) is seen at the operating bias and over the full temperature range, while for the higher bias, both diffusion and GR contributions are seen, at high and low temperature, respectively.

$J \propto T^3 e^{-\Delta E/k_B T}$, yielding an activation energy in each case of ΔE~336 meV. In Refs. 2, 6, and 7 it was shown that a correction of -36 meV must be added to this value in order to take the dependence of the bandgap on temperature into account and deduce the bandgap energy at 150K. This yields ΔE(150 K)~300 meV, which corresponds very well to the expected bandgap energy of 302 meV for lattice matched InAsSb[7]. It was also shown in Refs. 2 and 7 that the diffusion current can be used to deduce a value of ~700 ns for the minority carrier lifetime, and a value of ~ 50 μm for the bulk diffusion length.

(b) Optical properties

In Figure 6, the photoresponse curves of 300×300μm^2 C_pB_nn and nB_nn *bariodes* are compared at 150K. The onset

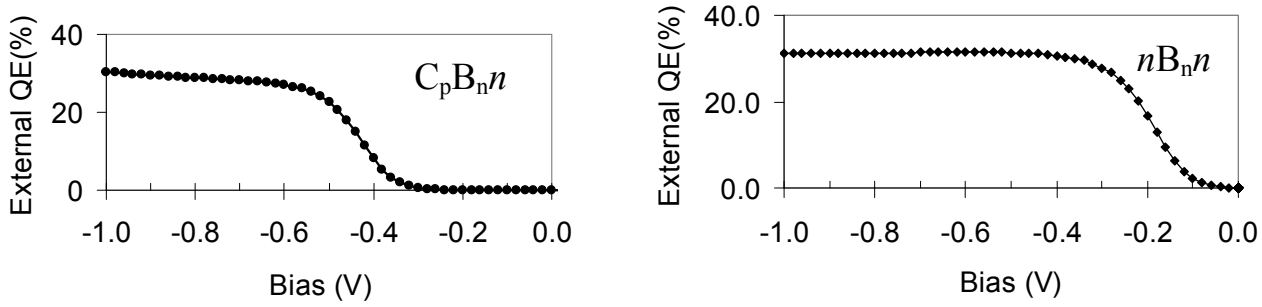

Figure 6
Photoresponse measured at 150K in the wavelength range 3.2-3.6μm range for (a) a C_pB_nn *bariode* and (b) an nB_nn *bariode*.

of saturation in the C_pB_nn *bariode* is delayed by about 0.3V, due to its larger operating bias. The saturation QE value of 30% agrees well with the calculated value assuming an internal QE of 100%. The unpolished substrate absorbs about 30% of the light, no antireflection coating was used, and the detectors were single pass devices. The method of calculation, based on an optical transfer matrix approach, has been described in detail in Ref. 6.

4. FOCAL PLANE ARRAYS

The results of the preceding sections show that our XB_nn *bariodes* exhibit a very low dark current and a very high internal quantum efficiency, making them very suitable for high performance staring FPAs. In this section we report QE and other radiometric measurements on Blue Fairy (BF) and Pelican FPA detectors made by bonding a 320×256/30μm pitch SCD BF ROIC or a 640×512/15μm pitch Indigo ISC0403 ROIC, respectively, to arrays of nB_nn *bariodes*. Results on C_pB_nn *bariodes* will be reported shortly.

Figure 7 compares the measured array average spectral response of a BF FPA (bold dotted curve) with the calculated response (bold solid curve). The calculation is based on the optical transfer matrix approach mentioned above[6]. An internal QE of 91% was used and the AL thickness of the detector was 2.6 μm. The optical thickness (*i.e.* thickness × refractive index) of the AR coating was t_{opt}=1.14 μm, which has a reflection minimum at $4t_{opt}$ = 4.6 μm. The shape of the spectral response

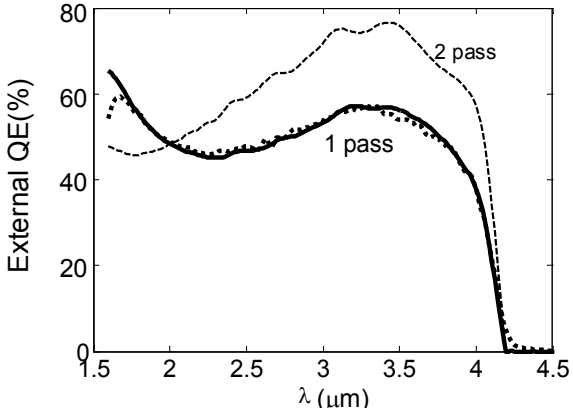

Figure 7
Optical transfer matrix simulation (thick solid line) of QE as a function of wavelength (spectral response) at 150K compared with the measured spectrum (thick dotted line) for a one pass nB_nn *bariode* detector with a 2.6 μm AL. The AR coating had an optical thickness of 1.14 μm. The thin dashed line is the result of a simulation where the optical thickness of the AR coating was optimized for the 3-4 μm wavelength range, and the reflectivity of the metal on top of the mesa was increased to give two pass operation. The internal QE used in the simulations was 91%.

curve is very sensitive to this parameter. For optimal performance, the AR coating thickness should be slightly reduced so that the reflection minimum occurs just after the initial rise of photoresponse. The detector in Figure 7 was a single pass device with a reflectivity of less than 20% from the metallization on the top of each mesa. We have developed a process which can increase this reflectivity to ~95% and allow two pass operation. To show the effect of this change and of using the optimized AR coating thickness, we performed a second calculation which incorporated these features. The result is shown by the thin dashed line labeled "2 pass" in Figure 7. The curve demonstrates that even with an AL thickness of only 2.6 μm, it is possible to achieve an average QE above 60% between 3 and 4 μm.

Figure 8 compares the measured spectral response of the FPA in Figure 7 (termed FPA 1 in the Figure) with that of another detector (FPA 2) which was purposely grown with a lattice mismatched AL in order to achieve a longer cut-off wavelength. This detector included a high reflectivity layer on the top of the mesa and had the same AL thickness as FPA 1.

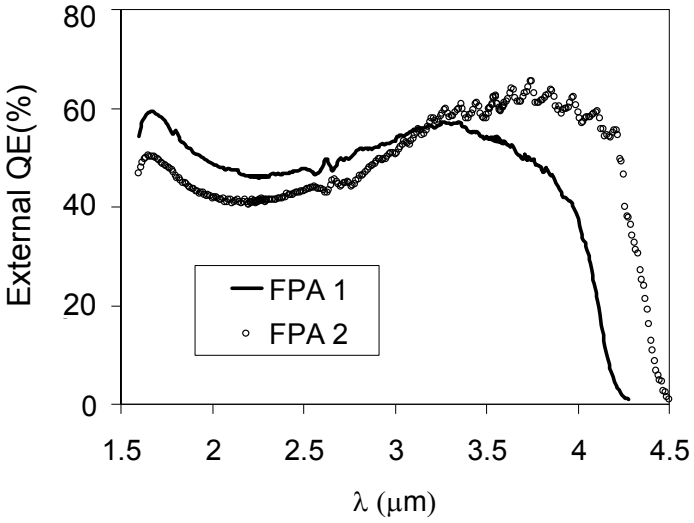

Figure 8
QE as a function of wavelength measured at 150K on two 30μm pitch $n\mathrm{B}_n n$ *bariode* BF FPAs with a 2.6 μm thick AL. In FPA1 (line) the AL was closely lattice matched to the substrate, while in FPA2 (circles) it was not.

In can be seen that the lattice mismatch leads to an increase in the cut-off wavelength of ~0.2 μm and the addition of the high reflectivity layer leads to an increase in the peak QE. The peak QE is not as high as that in the 2 pass calculation of Figure 7, because the fill factor of the highly reflecting layer was 75%, and the AR coating was not fully optimized. Nevertheless Figure 8 shows that a reasonable degree of wavelength tunability is possible, without sacrificing high QE.

The image quality and radiometric properties at 150K of a one pass $n\mathrm{B}_n n$ FPA bonded to a 30 μm pitch BF ROIC, were reported recently in Ref. 6. In the rest of this section we present an image and radiometric results for a $n\mathrm{B}_n n$ FPA with a 3 μm thick AL and an optimized AR coating thickness, bonded to a 15μm pitch ISC0403 ROIC. The map in Figure 9 shows the difference in the raw signals measured at 27 °C and 20 °C in this FPA, after dividing by a factor of $\cos^4\theta$, and normalizing to give an average value of 1. The factor of $\cos^4\theta$ represents the functional form of the light intensity distribution at the focal plane determined by the optical aperture, where θ is the angle subtended between a given pixel and the optical axis, at the centre of the aperture. The map shows good uniformity in the raw signal and a fairly even distribution of bad pixels. The bad pixels are shown as black points in Figure 9, and are those pixels with ≤75% or ≥125% of the average response. In total, there are about 1550 bad pixels, corresponding to an FPA operability of 99.5%

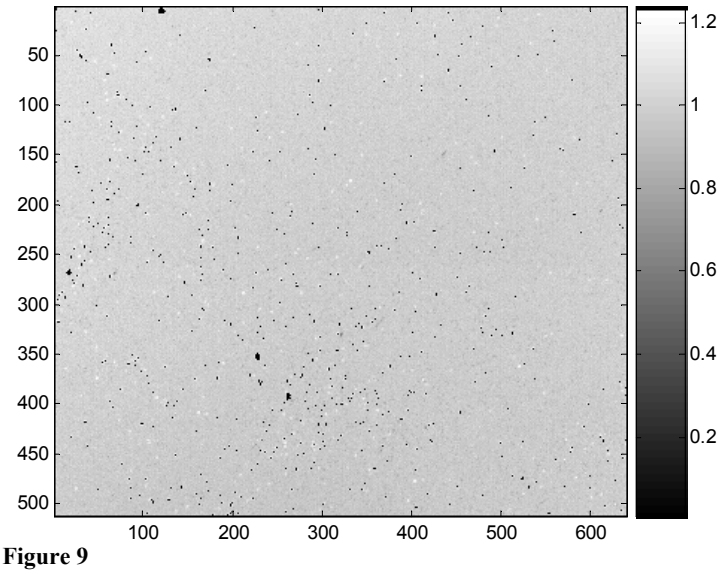

Figure 9
Raw Signal Difference map for black body temperatures of 27 °C and 20 °C, after dividing by a factor of $\cos^4\theta$, and normalizing to give an average value of 1.

Figure 10 shows an image at 150K from the FPA of Figure 9. The image was registered with an f/3.2 aperture, and the photocurrent to dark current ratio was >20. A stronger signal corresponds to a darker shade of grey. The small black features are cows grazing at a distance of less than a kilometer. The large black features are warm shades covering nearby street lights. The image was recorded with a two point non uniformity correction procedure, similar to that used in SCD's standard planar InSb detectors which operate at 77K. The measured average external QE was >70%. The image is still

background limited at 165K. The NETD measured at 150K and an integration time of 22 ms was 20 mK when the detector was placed in front of an extended 27°C black body. This value was limited only by shot and Read-Out noise.

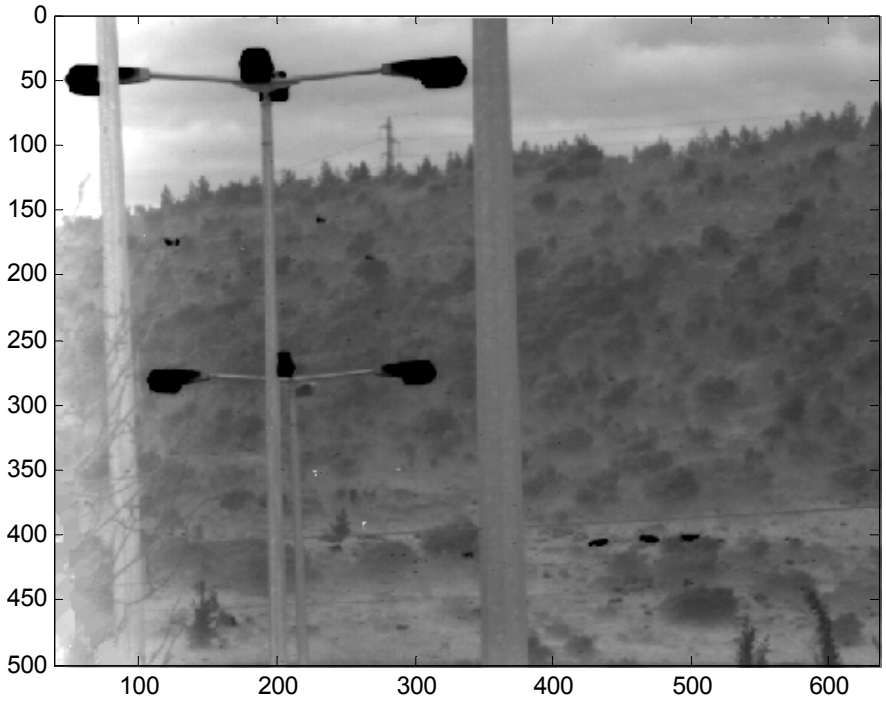

Figure 10
Image registered at 150K from the 640×512/15 μm pitch nB$_n$$n$ *bariode* Pelican FPA described in the text. The small dark objects are cows grazing in the field, and the range to the electricity pole at the top of the hill is about 2 Km.

5. SUMMARY AND CONCLUSIONS

We have shown that the suppression of the G-R current in XB$_n$$n$ *bariode* devices is a truly generic effect that does not depend on "X". Essentially the same dark current density and the same QE are obtained at the *bariode* operating bias, defined as the bias where the QE vs. V curve enters a plateau, regardless of whether X stands for p-GaSb (C_pB_nn *bariode*) or n-InAsSb (nB$_n$$n$ *bariode*). The heart of the device is the unipolar n-type Barrier and Active Layer region, which is made from n-AlSbAs/n-InAsSb, and is identical in both devices. The main effect of "X" is on the value of the operating bias. For p-GaSb, the magnitude of the operating bias is about 0.3V higher than for n-InAsSb, due to the different band alignments of the two materials.

The Active layer and Barrier layer are both n-type, because this ensures that no depletion occurs in the narrow bandgap photon absorbing layer. We have shown how important doping levels and layer thicknesses can be characterized quite effectively, using C-V profiling measurements. The minority carrier lifetime at 150K in the photon absorbing layer has been found to be ~700 ns, as determined from the temperature dependence of the dark current. This large value contributes to the very low detector dark currents and high BLIP operating temperatures of our XB$_n$$n$ *bariode* devices. The measured spectral response of a 30 μm pitch FPA, bonded to SCD's Blue Fairy ROIC agreed very well with an optical transfer matrix model that we have developed to simulate the detector performance. The model shows that the internal QE is greater than 90% and that an optimized 2 pass detector with a 2.6 μm Active layer will give an average QE of ~70% for black body radiation between wavelengths of 3 and 4 μm. By intentionally growing the Active layer lattice mismatched we were able to extend the detector cut-off wavelength by 0.2μm, while still maintaining a high QE and a low dark current.

We have fabricated a Pelican FPA from a 640×512/15μm pitch nB$_n$$n$ *bariode* array with a 3 μm Active layer thickness. The detector gives a good image at 150K, with an external QE of >70%, an operability of >99.5%, and an NETD, at f/3.2 and 22 ms integration time, of 20mK, limited only by shot and Read-Out noise. The detector shows BLIP performance up to an operating temperature of about 165K.

ACKNOWLEDGEMENTS

The material in this article is based on work partially supported by the Defense Advanced Research Projects Agency (DARPA) under contract No. HR0011-08-C-0063. Any opinions, findings and conclusions or recommendations expressed in this material are those of the authors and do not necessarily reflect the views of the Defense Advanced Research Projects Agency (DARPA), the U.S. Department of Defense (DoD) or the U.S. Government.

The authors would like to acknowledge technical support from Mr. S. Greenberg, who was responsible for the smooth operation of the MBE growth equipment, and Ms. B. Yariv, Ms. H. Moshe, Ms. H Schanzer, Mr. Y. Caracenti, Mr. D. Gur and Mr. S. Weinstein who have all contributed to the successful processing, packaging or characterization of the devices. We are grateful to Dr. Z. Calahorra for coining the term "*bariode*".

REFERENCES

[1] P.C. Klipstein, "Depletionless Photodiode with Suppressed Dark Current…" US Patent 7795640 (Filed: 2 July 2003)

[2] Philip Klipstein, Olga Klin, Steve Grossman, Noam Snapi, Inna Lukomsky, Michael Yassen, Daniel Aronov, Eyal Berkowitz, Alex Glozman, Tal Fishman, Osnat Magen, Itay Shtrichman, and Eliezer Weiss, "*XBn barrier Photodetectors based on InAsSb with high operating temperatures*", Journal of Optical Engineering, to be published (2011)

[3] P.C. Klipstein, "*X*B*n Barrier Photodetectors for High Sensitivity and High Operating Temperature Infrared Sensors*", Proc. Infrared Technology and Applications XXXIV, SPIE **6940**, 6940-2U (2008)

[4] In 1919, William Henry Eccles coined the term ***diode*** from the Greek roots *dia*, meaning "*through*", and *ode* (from *ὁδος*), meaning "*path*" (http://en.wikipedia.org/wiki/Diode#History). ***Bariode*** is a portmanteau of the term "***barrier diode***" that describes a semiconductor photo-detector in which a clear *path through* the device is provided for minority carriers from the photon absorbing layer, while the path of its majority carriers is blocked by means of a *barrier.* An *n*-type *bariode* has an *n*-type AL and BL, while in a *p*-type *bariode*, their polarities are reversed.

[5] Anthony White, "Infra Red Detectors" USA Patent 4,679,063 (Filed: 22 Sep 1983)

[6] P.C. Klipstein, O. Klin, S. Grossman, N. Snapi, B. Yaakobovitz, M. Brumer, I. Lukomsky, D. Aronov, M. Yassen, B. Yofis, A. Glozman, T. Fishman, E. Berkowicz, O. Magen, I. Shtrichman, and Eliezer Weiss, "*XBn Barrier Detectors for High Operating Temperatures*", Proc. Quantum Sensing and Nanophotonics Devices VII, SPIE **7608**, 7608-1V (2010)

[7] P.C. Klipstein, O. Klin, S. Grossman, N. Snapi, B. Yaakobovitz, M. Brumer, I. Lukomsky, D. Aronov, M. Yassen, B. Yofis, A. Glozman, T. Fishman, E. Berkowicz, O. Magen, I. Shtrichman, and Eliezer Weiss, "*MWIR InAsSb XBn Detectors for High Operating Temperatures*", SPIE Infrared Technology and Applications XXXVI **7660**, 7660-2Y (2010)

[8] D.W. Palmer in "*Growth and Characterisation of Semiconductors*" (eds. R.A. Stradling and P.C.Klipstein), Adam Hilger publisher (Bristol and New York) 187 (1990)